nature sustainability

ARTICLES

https://doi.org/10.1038/s41893-020-00635-w

Check for updates

# Organic wastewater treatment by a single-atom catalyst and electrolytically produced $H_2O_2$

Jinwei Xu[1], Xueli Zheng[1], Zhiping Feng[2], Zhiyi Lu[1], Zewen Zhang[1], William Huang[1], Yanbin Li[1], Djordje Vuckovic[3], Yuanqing Li[3], Sheng Dai[4], Guangxu Chen[1], Kecheng Wang[1], Hansen Wang[1], James K. Chen[2,5], William Mitch[3] and Yi Cui[1,6]✉

**The presence of organic contaminants in wastewater poses considerable risks to the health of both humans and ecosystems. Although advanced oxidation processes that rely on highly reactive radicals to destroy organic contaminants are appealing treatment options, substantial energy and chemical inputs limit their practical applications. Here we demonstrate that Cu single atoms incorporated in graphitic carbon nitride can catalytically activate $H_2O_2$ to generate hydroxyl radicals at pH 7.0 without energy input, and show robust stability within a filtration device. We further design an electrolysis reactor for the on-site generation of $H_2O_2$ from air, water and renewable energy. Coupling the single-atom catalytic filter and the $H_2O_2$ electrolytic generator in tandem delivers a wastewater treatment system. These findings provide a promising path toward reducing the energy and chemical demands of advanced oxidation processes, as well as enabling their implementation in remote areas and isolated communities.**

Advanced oxidation processes (AOPs), which produce highly reactive radicals ($OH^•$, $Cl^•$ and so on) from soluble oxidants ($H_2O_2$, $O_3$, HOCl and so on), are state-of-the-art water treatment technologies used for the removal of organic contaminants[1–3]. Radicals react rapidly and non-selectively with organic contaminants and ultimately mineralize them into harmless small molecules ($CO_2$, $H_2O$ and so on). However, despite the substantial development of AOPs since the concept was formally defined in 1987 by Glaze et al.[4], two fundamental challenges have thus far limited their practical use.

The first challenge in regard to AOPs is the efficient activation of $H_2O_2$. Ultraviolet (UV) light is widely used in commercialized AOPs to cleave the O-O bond of $H_2O_2$ to generate $OH^•$, yet this process is highly energy intensive[5]. Therefore, finding a catalyst to activate $H_2O_2$ without energy input is the crux of next-generation AOPs. Homogeneous catalysts, such as Fenton's reagent[6] (equations (1, 2)), suffer from drawbacks including the requirement of low pH, the recyclability of $Fe^{2+}$ and the accumulation of iron-containing sludge. Heterogeneous Fenton reaction is a promising alternative[7] (equations (3, 4)). Previous studies have mainly focused on activation of $H_2O_2$ through the one-electron redox cycle of exposed transition-metal atoms (Fe (ref. [8]), Cu (ref. [9]), Mn (ref. [10]) and so on) on various supports (magnetite[11], zeolites[12], activated carbon[13] and so on). However, few of these catalysts exhibit good activity at pH 7.0, which is often attributed to three factors: (1) the quenching of $OH^•$ by adjacent transition-metal atoms[8] (equations (3, 5)); (2) the disproportionation of $H_2O_2$ proceeding via a two-electron redox cycle[14] (equations (6, 7)); and (3) the slow kinetics of equation (4) retarding the full catalytic cycle[15].

$$Fe^{2+} + H_2O_2 \rightarrow Fe^{3+} + OH^• + OH^- \quad (1)$$

$$Fe^{3+} + H_2O_2 \rightarrow Fe^{2+} + OOH^• + H^+ \quad (2)$$

$$M^{n+}_{surface} + H_2O_2 \rightarrow M^{(n+1)+}_{surface} + OH^• + OH^- \quad (3)$$

$$M^{(n+1)+}_{surface} + H_2O_2 \rightarrow M^{n+}_{surface} + OOH^• + H^+ \quad (4)$$

$$M^{n+}_{surface} + OH^• \rightarrow M^{(n+1)+}_{surface} + OH^- \quad (5)$$

$$M^{n+}_{surface} + H_2O_2 \rightarrow M^{(n+2)+}_{surface} + 2OH^- \quad (6)$$

$$M^{(n+2)+}_{surface} + H_2O_2 \rightarrow M^{n+}_{surface} + O_2 + 2H^+ \quad (7)$$

Note that $M_{surface}$ denotes surface transition-metal atoms. The second challenge with AOPs is the sustainable production of $H_2O_2$. The current industrial anthraquinone process requires complex infrastructure and is not feasible for small-scale operations[16]. Besides, the hazards associated with the transportation and storage of $H_2O_2$ further hinder the implementation of AOPs in remote areas and isolated communities. A promising alternative route is the on-site generation of $H_2O_2$ via the two-electron reduction of $O_2$ (2e-ORR) (equation (8)). This process can be coupled with the oxygen evolution reaction (OER) (equation (9)) to produce $H_2O_2$ in an electrolysis device from air, water and renewable energy (equation (10)). Substantial efforts have been invested in catalyst development and mechanistic studies for 2e-ORR[17–20], yet few device-level demonstrations have shown its practical utility[21–24].

[1]Department of Materials Science and Engineering, Stanford University, Stanford, CA, USA. [2]Department of Chemical and Systems Biology, Stanford University School of Medicine, Stanford, CA, USA. [3]Department of Civil and Environmental Engineering, Stanford University, Stanford, CA, USA. [4]Department of Materials Science and Engineering, University of California Irvine, Irvine, CA, USA. [5]Department of Developmental Biology, Stanford University School of Medicine, Stanford, CA, USA. [6]Stanford Institute for Materials and Energy Sciences, SLAC National Accelerator Laboratory, Menlo Park, CA, USA. ✉e-mail: yicui@stanford.edu

$$O_2 + 2e^- + 2H^+ \rightarrow H_2O_2\ E_{red} = 0.695\ \text{V versus RHE} \quad (8)$$

$$2H_2O \rightarrow O_2 + 4H^+ + 4e^-\ E_{red} = 1.229\ \text{V versus RHE} \quad (9)$$

$$O_2 + 2H_2O \xrightarrow{0.534\ \text{V}} 2H_2O_2 \quad (10)$$

Note that $e^-$ denotes electrons and $E_{red}$ denotes reduction potential. Here we present a wastewater treatment system that successfully tackles the two aforementioned scientific challenges in regard to current AOPs. This system is enabled by two key innovations: first, we report that Cu single atoms incorporated in graphitic carbon nitride ($C_3N_4$) solve all three challenges in regard to current heterogeneous Fenton catalysts and show superb activity in activation of $H_2O_2$ to generate $OH^•$ at pH 7.0. We further demonstrate the immobilization of the catalyst in a Fenton filter, which bypasses the redundancy of catalyst recovery. Second, we report the design of an electrolysis device that produces 10 g $l^{-1}$ $H_2O_2$ at a total cost of US$4.66 per $m^3$ by consuming air, electricity and 0.1 M $Na_2SO_4$ electrolyte. This device is based on (1) a novel gas diffusion electrode (GDE) to provide sufficient three-phase catalytic interfaces, (2) a three-chamber design for operation within a continuous flow reactor, (3) a carbon-based material recently reported[17] to catalyse 2e-ORR, (4) anodically electrodeposited $IrO_2$ to catalyse OER and (5) careful selection of the electrolyte used. The Fenton filter and $H_2O_2$ electrolyser work in tandem to deliver the wastewater treatment system. We further demonstrate a $Fe_3O_4$-carbon filter that quenches residual $H_2O_2$ and renders the effluent safe for discharge into the environment. Small-scale pilot studies have demonstrated the feasibility of the whole system.

## Results

The schematic of our wastewater treatment system is shown in Fig. 1, and includes five steps: (1) $H_2O_2$ electrolysers generate $H_2O_2$ in a 0.1 M $Na_2SO_4$ solution by consuming electricity and air; (2) the resultant $H_2O_2$ solution is added to the wastewater and mixed thoroughly; (3) the mixed solution flows through a Fenton filter where organic contaminants are oxidized; (4) the solution further flows through a $Fe_3O_4$-carbon filter where the residual $H_2O_2$ is quenched; and (5) the treated effluent is discharged into the environment. The Fenton filter and $H_2O_2$ electrolyser are at the heart of this system and solve the activation and production of $H_2O_2$, respectively. In the following sections we first discuss the design considerations and performance of the two components in parallel with correlation of the $H_2O_2$ concentration (applied or generated), and in the final section we demonstrate the feasibility of the entire system in regard to treatment of synthetic wastewater.

**Single-atom catalyst and design considerations.** Concerning heterogeneous Fenton reaction, the most desirable feature provided by single-atom catalysts is the uniform dispersion of active sites in loose proximity to one another, which restrains the catalyst itself from quenching $OH^•$ (equation (5)). Therefore, we synthesized Cu-incorporated $C_3N_4$ (Cu-$C_3N_4$) (Fig. 2a) via a simple one-pot method (Methods), with $Cu(NO_3)_2$ and cyanamide (mole ratio 1:20) serving as the precursor. The Cu content in Cu-$C_3N_4$ can be readily tailored by altering the mole ratio of Cu:C in the precursor. The morphology of Cu-$C_3N_4$ was characterized by aberration-corrected high-resolution transmission electron microscopy (HR-TEM). As seen in Fig. 2b, the catalyst material consists of a homogeneous amorphous structure without the presence of Cu or CuO nanoparticles. Elemental mapping (Supplementary Fig. 1) by energy-dispersive X-ray spectroscopy (EDS) suggests the existence and uniform concentration of Cu over the $C_3N_4$ matrix. Closer observation, using aberration-corrected high-angle annular dark-field scanning transmission electron microscopy (HAADF-STEM), revealed the sole presence of isolated Cu atoms (circled in Fig. 2c). We subsequently employed Cu K-edge extended X-ray absorption fine structure spectroscopy (EXAFS) to confirm the coordination environment of Cu atoms. Unlike Cu, $Cu_2O$ and CuO, our Cu-$C_3N_4$ shows negligible Cu–Cu interaction based on analysis of its Fourier-transformed EXAFS spectra (Fig. 2d), which is required to avoid the radical-quenching problem mentioned above. A further comparison between Cu-$C_3N_4$ and Cu-TMCPP (structural formula shown in Supplementary Fig. 2) on their EXAFS spectra shows that they share the same main peak centred around 1.5 Å, corresponding to Cu–N coordination.

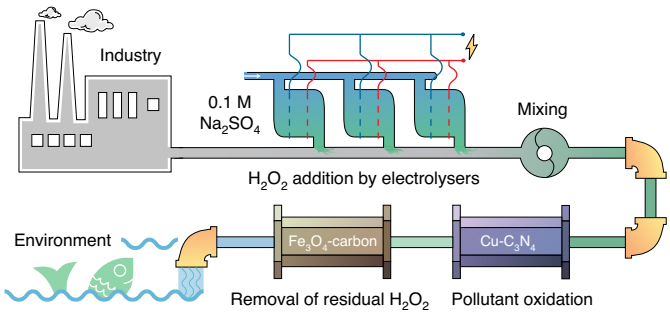


**Fig. 1 | Schematic drawing of our wastewater treatment system.** The system includes the $H_2O_2$ electrolyser, the Fenton filter and the $Fe_3O_4$-carbon filter.

The reason for choosing Cu and $C_3N_4$ as the active centre and hosting matrix, respectively, is that this combination provides redox sites with single-electron capacity, which favours the radical mechanism (equation (3)) over the non-radical mechanism (equation (6)) during decomposition of $H_2O_2$. In order to support this hypothesis, we probed the electronic properties of Cu-$C_3N_4$ by X-ray photoelectron spectroscopy (XPS) (Fig. 2e). As expected, the Cu LMM Auger spectrum confirmed the absence of metallic Cu(0), and the two peaks at 932.4 and 934.6 eV in the Cu 2p spectrum can be assigned to Cu(I) and Cu(II), respectively, indicating that Cu single atoms can act as the desired redox sites with single-electron capacity. We further compared the N 1s and C 1s spectra of Cu-$C_3N_4$ with those of undoped $C_3N_4$ (Supplementary Fig. 3) and found negligible differences, which indicates that the introduction of Cu into the precursor does not affect the formation of $C_3N_4$. Fourier-transformed infrared spectroscopy (FTIR) was also introduced to ascertain the local structure (Fig. 2f). In particular, the band at 1,314 $cm^{-1}$, corresponding to the vibration of C=N−C (ring N), is less pronounced in the spectrum of Cu-$C_3N_4$ while that at 1,228 $cm^{-1}$, corresponding to the vibration of N−$(C)_3$ (tertiary N), shows similar intensity in the two spectra[25,26]. These results support the EXAFS spectra, suggesting coordination of Cu atoms by $C_3N_4$ via the ring N sites. In summary, isolated Cu atoms with single-electron redox capacity were successfully incorporated into the N-coordinating cavities of $C_3N_4$.

**$H_2O_2$ activation by Cu-$C_3N_4$.** To evaluate the activity of Cu-$C_3N_4$ as a heterogeneous Fenton catalyst, we used the oxidative degradation of rhodamine B (RhB) as a model reaction. As shown in Fig. 3a, degradation of RhB in the Cu-$C_3N_4$/$H_2O_2$ suspension reached 99.97% in only 5 min while <40% of RhB was removed when using conventional Cu-containing catalysts such as $Cu_2O$ or CuO. In addition, dissolved $Cu^{2+}$ showed negligible homogeneous catalytic activity at pH 7.0. Further insights into catalytic activity were obtained by assessing the influence of Cu content in Cu-$C_3N_4$. As shown in Supplementary Fig. 4a, reducing Cu content reduced catalytic activity, suggesting that Cu is the active site. On the other hand, excessive Cu in the precursor adversely affected catalyst performance due to

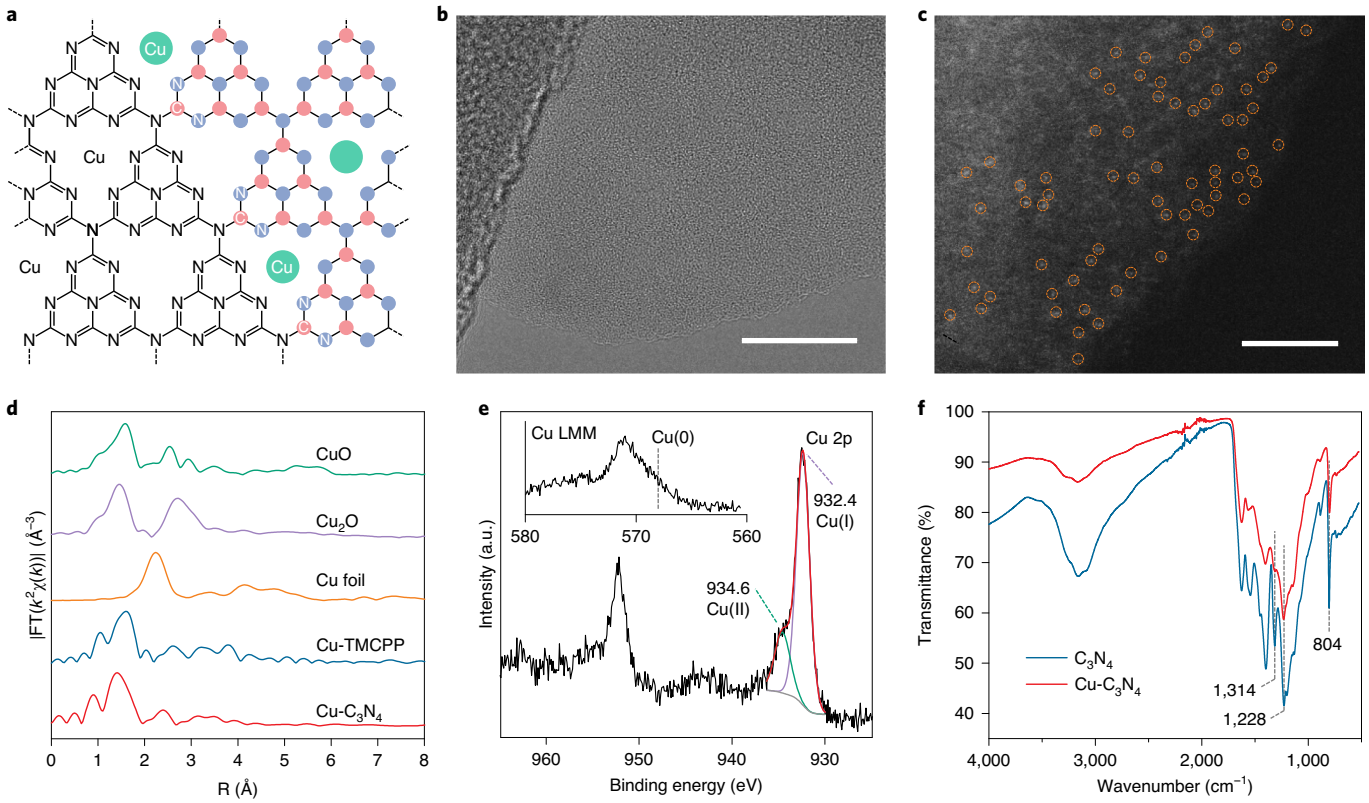


**Fig. 2 | Characterization of Cu-$C_3N_4$.** **a**, Structural illustration of Cu-$C_3N_4$. **b**, Aberration-corrected HR-TEM image of Cu-$C_3N_4$ showing the absence of crystalline structure. The darker area in the top-left corner is due to the lacey carbon of the TEM grid. Scale bar, 20 nm. **c**, Aberration-corrected HAADF-STEM image of Cu-$C_3N_4$. Circles indicate single Cu atoms. Scale bar, 2 nm. **d**, Normalized $k^2$-weighted Fourier transform (FT) of the EXAFS spectra of Cu-$C_3N_4$ and other reference materials within radial distance. **e**, XPS Cu 2p spectrum and Cu LMM Auger spectrum (inset) of Cu-$C_3N_4$. The black lines denote the raw data while the coloured lines correspond to the deconvoluted components. **f**, FTIR spectra of Cu-$C_3N_4$ and undoped $C_3N_4$. a.u., arbitrary units.

the formation of CuO nanoparticles (Supplementary Fig. 4b). This observation supports our catalyst design considerations, that isolated single atoms are preferable to metal oxide nanoparticles when activating $H_2O_2$ to generate $OH^{\bullet}$.

To highlight the exceptional stability of Cu-$C_3N_4$, the RhB degradation tests were repeated for ten cycles (Supplementary Fig. 5a). Its pseudo-first-order reaction rate decreased from 1.64 to 1.08 $min^{-1}$ over the first five cycles but stabilized thereafter. XPS analysis (Supplementary Fig. 5b) revealed that the relative ratio of Cu(I):Cu(II) in the used catalyst differed from that in fresh Cu-$C_3N_4$, which supports our hypothesis that the Cu(I)/Cu(II) redox is involved in the catalytic process. Comparison of EXAFS spectra (Supplementary Fig. 5c) between used and fresh catalysts confirmed the preservation of the single-atomic dispersion after cycles of reaction.

To identify the degradation products of RhB, we applied liquid chromatography-mass spectrometry (LC–MS). Figure 3b presents the chromatograms of a 10-μM RhB solution at different degradation times. The notable peaks are labelled with the corresponding $m/z$ values as measured by mass spectrometry. The peak with $m/z = 443$ at retention time 4.4 min relates to RhB, which decayed with increasing degradation time and finally disappeared after 5 min. This observation is consistent with the results shown in Fig. 3a. A probable degradation pathway (Supplementary Fig. 6) is proposed based on the analysis of other major peaks in LC–MS chromatograms[27,28]. All peaks disappeared after 1 h of degradation, indicating that all intermediate products were mineralized to $CO_2$. The pH of the solution decreased from 7.0 to 5.4 after the 1-h experiment, which also implies the production of $CO_2$.

To further confirm the degree of mineralization, we measured the removal of total organic carbon (TOC) during the degradation. Due to the TOC detection limit (0.1 ppm), we increased the initial RhB concentration from 10 to 50 μM, with the concentrations of Cu-$C_3N_4$ and $H_2O_2$ still kept at 1 $g l^{-1}$. As shown in Fig. 3c, 73% of TOC remained after 25 min when all RhB had been completely degraded. Then, the removal rate of TOC gradually increased and a mineralization degree of 95% was reached after 1 h. The increasing TOC removal rate agrees with the proposed degradation pathway, indicating that mineralization undergoes two different stages[29]: (1) scission of RhB molecules and (2) subsequent oxidation of fragments. We also analysed the inorganic nitrogen species produced during degradation (Supplementary Fig. 7) and found that nearly 90% of the amine groups in RhB were converted into inorganic species after 1 h, with $NH_4^+$ as the main mineralization end product.

**Fenton filter.** The high catalytic activity of Cu-$C_3N_4$ encouraged us to further explore its scope at the device level. Figure 4a shows an image taken of a proof-of-concept Fenton filter. Specifically, a square tube of cross-sectional area 1 $cm^2$ and length 5 cm was filled with carbon felt, which is a porous structure composed of carbon fibres. Cu-$C_3N_4$ was coated on the surface of each carbon fibre, as shown in the scanning electron microscopy (SEM) image in Fig. 4b. A mixed solution of 10 ppm RhB and 1 $g l^{-1}$ $H_2O_2$ was passed through the Fenton filter at a flow rate of 10 $ml h^{-1}$. As shown in Fig. 4c, the Fenton filter maintained 100% dye removal efficiency after 200 h of operation (2 l of wastewater was filtered). The TOC in the effluent was below the detection limit (0.1 ppm) throughout

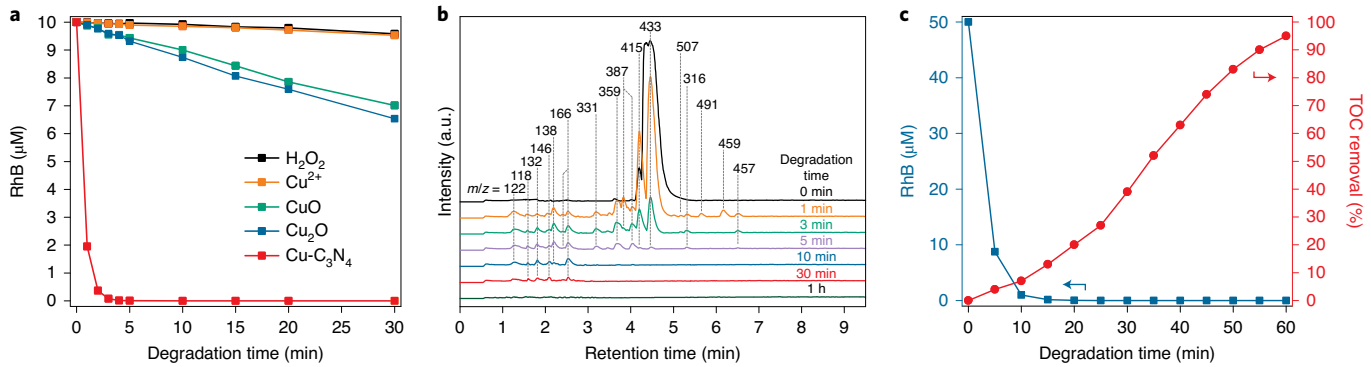


**Fig. 3 | Catalytic activity and degradation product. a**, Degradation of 10 μM RhB in the presence of 1 g $l^{-1}$ $H_2O_2$ and selected catalysts. Reaction conditions were 10 ml of aqueous solution, 1 g $l^{-1}$ catalyst (if present), pH 7.0 (adjusted to 7.0 at the beginning of the reaction without buffer control). **b**, LC–MS chromatograms of the reaction solution at different degradation time intervals. The reaction conditions are the same as those in **a**, with Cu-$C_3N_4$ as the catalyst. **c**, TOC removal during the degradation of 50 μM RhB in the presence of 1 g $l^{-1}$ $H_2O_2$ and 1 g $l^{-1}$ Cu-$C_3N_4$. Reaction conditions were 100 ml of aqueous solution, pH 7.0.

the course of the experiment, confirming the complete oxidation of the dye molecules. At 100 h, we changed the pollutant from 10 ppm RhB to 10 ppm methylene blue (MB) to demonstrate the versatility of our Fenton filter for different pollutant molecules. A video of the filtration process is shown in Supplementary Video.

A major advantage of using Cu-$C_3N_4$ lies in its leaching resistance. Inductively coupled plasma mass spectrometry was carried out to measure the concentration of leached Cu in the effluent. As illustrated by the blue curve in Fig. 4c, the Cu concentration in the effluent finally reached a steady state of 0.1 ppm, which is well below the goal of maximum contamination for drinking water (1.3 ppm) set by the US Environmental Protection Agency. Because the relatively high concentration of Cu in the initial effluent can be attributed to unreacted precursors, washing the filter with water after synthesis would help reduce this leaching. Further insights into the treatment capacity of the Fenton filter were obtained by varying the flow rate and $H_2O_2$ dosage (see further details in Supplementary Fig. 8).

Up to this point we had successfully developed a Fenton filter that can remove organic contaminants from a mixed solution of wastewater and $H_2O_2$ and with no energy input—the only chemical input is $H_2O_2$. To further eliminate the dependence of the treatment system on $H_2O_2$, we developed a $H_2O_2$ electrolyser for the on-site generation of $H_2O_2$ from air, water and renewable energy. The following two sections are devoted to discussion of this electrolyser.

**Electrodes and electrolytes of the $H_2O_2$ electrolyser.** The major challenge in developing a $H_2O_2$ electrolyser regards the cathode for 2e-ORR. Because the ratio of $O_2$ to $H_2O$ molecules in an aqueous solution under atmosphere is only ~1:200,000, it is very easy for a conventional cathode immersed in electrolyte to reach the diffusion limit and build up a high concentration over-potential. The schematic in Fig. 5a shows our design of a GDE developed to solve this problem by directly delivering the gas reactant to the catalyst surface. We fabricated the GDE by mixing melted polyethylene (PE) and paraffin oil, then melt-pressing the composite mixture with a carbon paper and finally extracting the paraffin oil with methylene chloride. Oxidized Super P carbon black (O-SP) was drop-cast on the carbon paper side of the GDE with a loading of 0.5 mg $cm^{-2}$. In this configuration, the carbon paper acts as the current collector, the porous PE functions as the hydrophobic gas diffusion layer, and the O-SP is the catalyst for 2e-ORR. $O_2$ is supplied from the porous PE side and reacts at the gas–catalyst–electrolyte interface. The cross-sectional SEM image in Fig. 5b shows that our GDE has a hierarchical structure. The larger pores (~50 μm) in the carbon

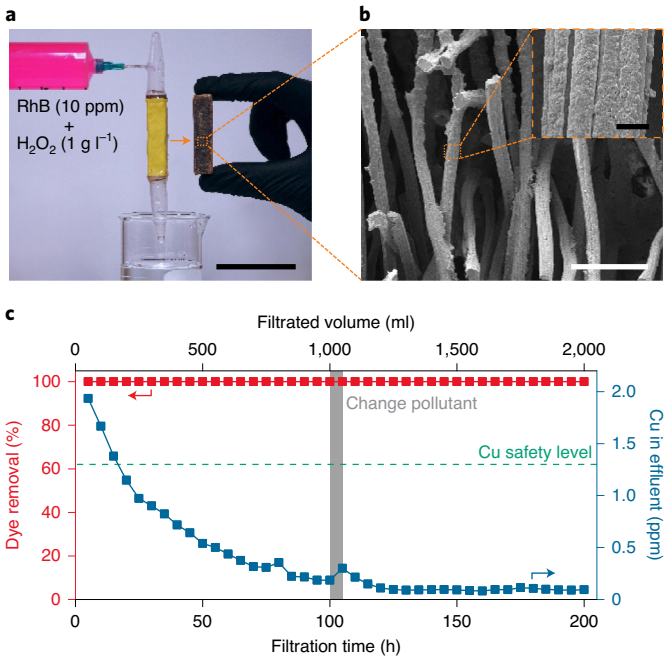


**Fig. 4 | Fenton filter. a**, Image of a proof-of-concept Fenton filter: cross-sectional area, 1 $cm^2$; length, 5 cm. Scale bar, 5 cm. **b**, SEM image of the filter medium. Scale bar, 100 μm. Inset, magnified SEM image showing the Cu-$C_3N_4$ catalyst coated on the surface of a carbon fibre. Scale bar, 5 μm. **c**, Dye removal and Cu concentration in effluent as functions of filtration time. Flow rate, 10 ml $h^{-1}$; contact time, 30 min; $H_2O_2$ dosage, 1 g $l^{-1}$. Pollutant, 10 ppm RhB for the first 100 h then 10 ppm MB for the second 100 h.

paper (Supplementary Fig. 9a) facilitate mass transport in the liquid phase while the smaller pores (~2 μm) in porous PE (Fig. 5c and Supplementary Fig. 9a) provide the gas diffusion pathway and prevent flooding.

The performance of the GDE was characterized using a three-electrode configuration in a custom H-type cell (Supplementary Fig. 10). We compare our GDE with an immersed carbon paper electrode using Tafel plots (Fig. 5d), which are converted from the linear sweep voltammetry (LSV) data shown in Supplementary Fig. 9c. For the immersed electrode with pure $O_2$

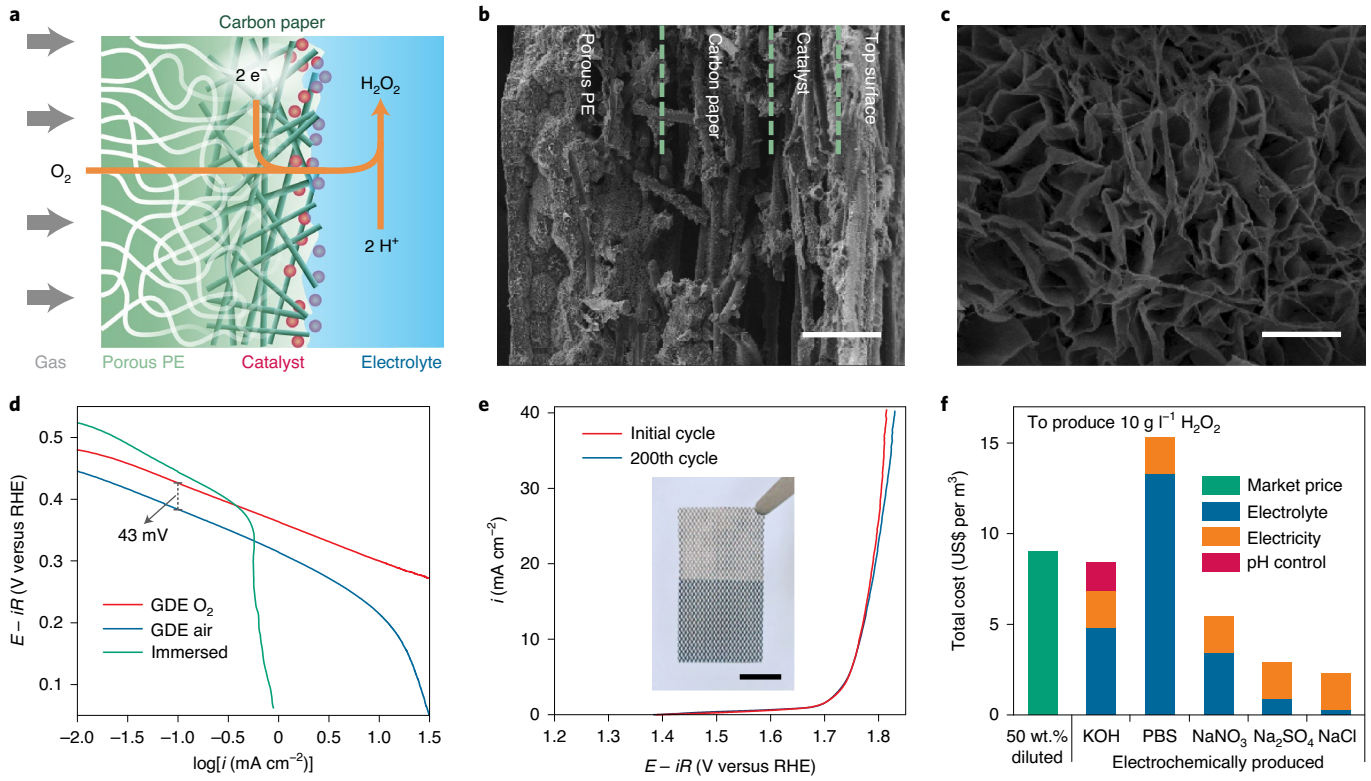


**Fig. 5 | Electrodes and electrolytes of $H_2O_2$ electrolyser. a**, Schematic drawing of the GDE for 2e-ORR. $O_2$ diffuses in the gas phase through the porous PE to the gas–catalyst–electrolyte interface and is then reduced by electrons transported from the carbon paper. **b**, Cross-sectional SEM image of the GDE, with dashed lines denoting the boundaries between components. The top surface is visible because the sample is slightly tilted. Scale bar, 50 μm. **c**, Magnified SEM image of the porous PE showing interconnected micron-sized pores, which provide the gas diffusion pathway and prevent flooding. Scale bar, 2 μm. **d**, Comparison of the Tafel plots of a GDE supplied with pure $O_2$, a GDE supplied with atmospheric air and a carbon paper electrode immersed in electrolyte. All the electrodes were loaded with the same amount of catalyst (0.5 mg cm$^{-2}$). Electrolyte, 0.1 M $Na_2SO_4$. **e**, LSV curves of the $IrO_2$ anode before and after 200 cycles of continuous CV scanning in 0.1 M $Na_2SO_4$. Inset, image of the $IrO_2$ anode. Scale bar, 5 mm. **f**, Cost estimate for producing 10 g l$^{-1}$ (1 wt.%) $H_2O_2$ solution using different electrolytes (0.1 M), based on the condition that both electrodes are operated at 20 mA cm$^{-2}$. The market price shown here is 2% of that for 50 wt.% $H_2O_2$.

directly bubbled into the electrolyte, the Tafel plot drops from linearity at 0.3 mA cm$^{-2}$, indicating depletion of $O_2$ adjacent to the electrode. In contrast, for our GDE with pure $O_2$ supplied from the porous PE side, the Tafel plot remains linear up to 30 mA cm$^{-2}$, confirming the sufficient delivery of $O_2$ to the catalyst. We further substituted air for pure $O_2$ to determine whether our GDE can operate without a supply of pure $O_2$. Although the Tafel plot deviates from linearity at high current density, 30 mA cm$^{-2}$ is still accessible at a reasonable over-potential. The overall potential shift of 43 mV marked in Fig. 5d is due to the lower partial pressure of $O_2$ in air, which is expected according to the Nernst equation. Another important attribute of the cathode is 2e-ORR selectivity relative to the four-electron reduction of $O_2$ to $H_2O$. As shown in Supplementary Fig. 9d, our GDE has a high 2e-ORR selectivity no matter whether $O_2$ is supplied in its pure state or in the form of air.

In addition to the cathode design, the anode must also be active and stable for OER. Here, we fabricated the anode by anodically electrodepositing $IrO_2$ on a titanium screen mesh in an oxalate-based deposition solution[30]. The inset of Fig. 5e shows a photo of the anode; the black colour of its lower part indicates the $IrO_2$ coating. The OER activity of our anode is confirmed by the LSV curve as shown in Fig. 5e. Moreover, the LSV curve after 200 cycles of continuous cyclic voltammetry (CV) scanning shows negligible difference from the initial one. To further confirm the stability of our cathode and anode, we conducted successive chronopotentiometry tests at 10, 20 and 30 mA cm$^{-2}$ (Supplementary Fig. 11). Both electrodes were very stable and showed no performance decay after 15 h of operation.

As stated above, the targeted $H_2O_2$ concentration in the mixed solution flowing through the Fenton filter is 1 g l$^{-1}$. Considering that a tenfold dilution is reasonable when mixing the electrolytically produced $H_2O_2$ solution into wastewater, the electrolyser needs to generate $H_2O_2$ at a concentration of 10 g l$^{-1}$. According to the potential of both electrodes at 20 mA cm$^{-2}$ and the selectivity of the cathode, we have an initial estimate of the electricity cost: US$2.03 per m$^3$. Compared with the market price of 10 g l$^{-1}$ $H_2O_2$ (US$9.00 per m$^3$, which is 2% of the market price of 50 wt.% $H_2O_2$), this electricity cost is very promising. However, a considerable additional cost comes from the electrolyte, which is a key component of an electrolyser yet is often neglected. Figure 5f summarizes the total cost for producing 10 g l$^{-1}$ $H_2O_2$ solution using different electrolytes (0.1 M). Although alkaline electrolyte provides a more stable condition for both OER and 2e-ORR, the cost of KOH and pH control suggests the need to sacrifice the activity of the catalysts for overall cost efficiency. In regard to pH-neutral electrolytes, phosphate-buffered saline (PBS) is too expensive, NaCl can be oxidized to chlorine at the anode and $NaNO_3$ is a concern regarding discharge to the environment. Therefore, we chose 0.1 M $Na_2SO_4$ as the electrolyte, with an estimated total cost of only US$2.93 per m$^3$.

**Reactor design and performance of the $H_2O_2$ electrolyser.** The $H_2O_2$ electrolyser is composed of three chambers (Fig. 6a).

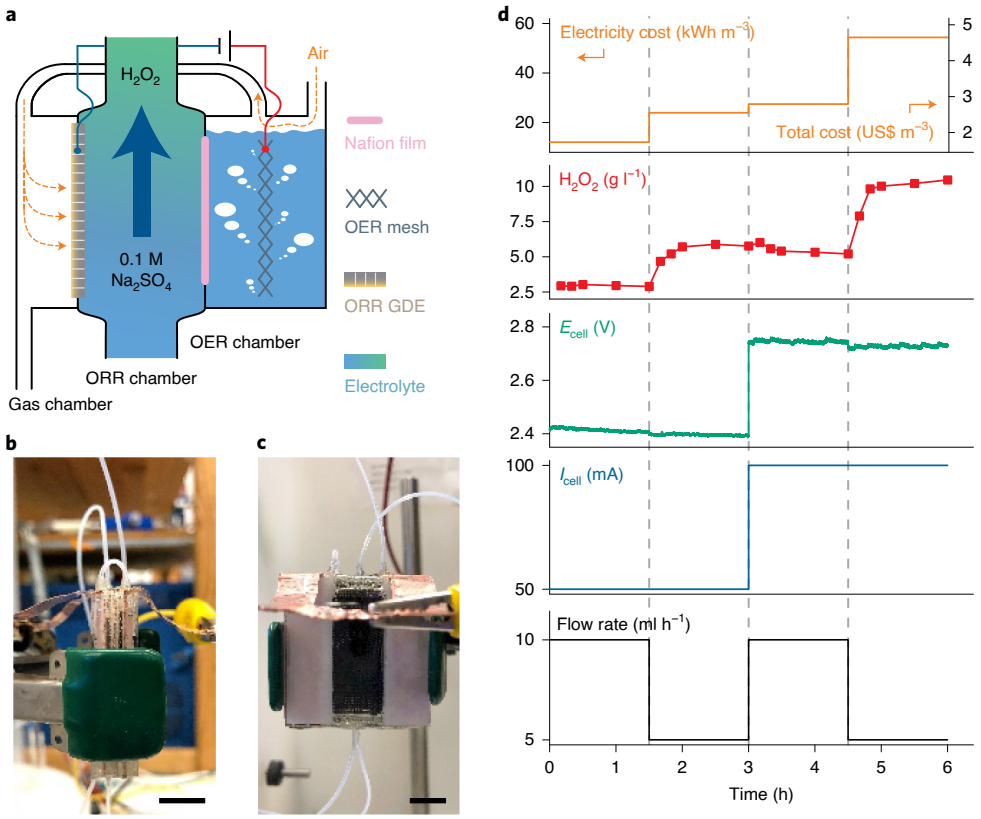


**Fig. 6 | Reactor design and performance of the $H_2O_2$ electrolyser. a**, Schematic drawing of the $H_2O_2$ electrolyser. **b**, Front-view image (the same view direction as the schematic). Scale bar, 1 cm. **c**, Side-view image (from the OER chamber side). Scale bar, 1 cm. **d**, Operation of the electrolyser by controlling the working current and electrolyte flow rate. Air flow was maintained at 10 ml $min^{-1}$. A 10 g $l^{-1}$ $H_2O_2$ solution was produced at a total cost of US$4.66 per $m^3$ when the working current and electrolyte flow rate were 100 mA and 5 ml $h^{-1}$, respectively.

An $IrO_2$-coated titanium mesh is immersed in the electrolyte in the OER chamber as the anode. The OER chamber is separated from the ORR chamber by a Nafion film, which allows proton migration and obstructs $H_2O_2$ diffusion. A GDE seals the other side of the ORR chamber, separating it from the gas chamber. A gas tube connects the tops of the OER and gas chambers. Atmospheric air is blown into the OER chamber, carrying the generated oxygen, and then flows through the gas chamber. $O_2$ diffuses through the GDE as stated above and is reduced to $H_2O_2$; 0.1 M $Na_2SO_4$ electrolyte then flows through the ORR chamber and carries out the resultant $H_2O_2$. Figure 6b,c provides front view (the same view direction as the schematic) and side view (from the OER chamber side) images, respectively, of the $H_2O_2$ electrolyser. The cathode and anode are both $1.5 \times 3.0$ $cm^2$.

We ran the electrolyser by controlling both working current and electrolyte flow rate (Fig. 6d), and the steady potential confirmed its stable operation. A 10 g $l^{-1}$ $H_2O_2$ solution was produced when the working current and electrolyte flow rate were maintained at 100 mA and 5 ml $h^{-1}$, respectively. The total cost (electricity plus electrolyte) of producing this $H_2O_2$ solution was US$4.66 per $m^3$, which is higher than the previous estimate because of impedance loss and the self-decomposition of $H_2O_2$. Nevertheless, this value is still lower than the market price and on-site generation further eliminates the cost associated with the transportation and storage of $H_2O_2$.

**Organic wastewater treatment system.** We combine the two aforementioned inventions, the Fenton filter and the $H_2O_2$ electrolyser, to present an organic wastewater treatment system. In order to quench residual $H_2O_2$ and thus render the effluent safe for discharge to the environment, we fabricated a $Fe_3O_4$-carbon filter via a process similar to that used to create the Fenton filter. It has the same exterior appearance as the Fenton filter yet is loaded with a different catalyst (Supplementary Fig. 12a,b). Specifically, $Fe_3O_4$ nanoparticles embedded in amorphous carbon (Supplementary Fig. 12c,d) were synthesized and immobilized on the filter medium to catalyse the disproportionation of $H_2O_2$. To characterize the performance of the filter in removal of $H_2O_2$, we passed a 1 g $l^{-1}$ $H_2O_2$ solution through the filter at a flow rate of 3 ml $h^{-1}$ and recorded the $H_2O_2$ concentration in the effluent. The $Fe_3O_4$-carbon filter demonstrated a very high $H_2O_2$ removal efficiency (>99.9%) over 100 h of operation (Supplementary Fig. 12e).

We investigated the feasibility of the whole system to treat synthetic wastewater containing a mixture of 10 ppm triclosan (antiseptic), 10 ppm 17α-ethinyl oestradiol (oestrogenic birth control medication) and 10 ppm cefazolin sodium (antibiotic). A $H_2O_2$ electrolyser was operated at a working current of 100 mA and electrolyte flow rate of 5 ml $h^{-1}$, generating ~10 g $l^{-1}$ $H_2O_2$ in a 0.1 M $Na_2SO_4$ solution. This solution was mixed with synthetic wastewater at a volume ratio of 1:9. The mixed solution was flowed through a Fenton filter at a flow rate of 3 ml $h^{-1}$ and then through a $Fe_3O_4$-carbon filter at a flow rate of 3 ml $h^{-1}$. We ran the system for 100 h continuously, treating 270 ml of synthetic wastewater and generating 300 ml of effluent. We measured the TOC in the effluent and found that all three organic contaminants were completely oxidized to $CO_2$. The residual $H_2O_2$ in the effluent was also confirmed to be below the detection limit (0.05 ppm). We further conducted a zebrafish embryo teratogenicity analysis (Supplementary Fig. 13) to

corroborate that our treatment system did not generate obviously toxic by-products.

## Discussion

In this article we present strategies to address the two fundamental challenges of AOPs: the activation and production of $H_2O_2$. First, we carried out a comprehensive study to highlight the technological potential of single atoms stabilized in appropriate hosts for heterogeneous Fenton reaction. The uniform dispersion of active sites in loose proximity to one another restrains the single-atom catalyst per se from quenching OH•, which is the key problem in regard to conventional heterogeneous Fenton catalysts. We identified Cu-$C_3N_4$ as a good catalyst at pH 7.0 and further demonstrated a Fenton filter by immobilizing the catalyst on a porous substrate, which eliminates the redundancy of catalyst recovery. Second, we fabricated a $H_2O_2$ electrolyser that can continuously produce a pH-neutral 10 g $l^{-1}$ $H_2O_2$ solution at a total cost of US$4.66 per $m^3$, by consuming only air, electricity and 0.1 M $Na_2SO_4$ electrolyte, which makes it practical for on-site production and a broad array of decentralized applications. The high level of performance is attributed to the intrinsic activities of the catalysts, the novel GDE and the three-chamber flow reactor design. Finally, we coupled the Fenton filter and $H_2O_2$ electrolyser in tandem and demonstrated a system for organic wastewater treatment. We note that additional efforts are needed to scale up the whole process; until then, we can assess its full potential by quantitatively benchmarking it with established industrial technologies. In Supplementary Discussion we identify the existing limitations of the wastewater treatment system (for example, the high $H_2O_2$/TOC ratio, the expensive OER catalyst, the sulfate remaining in the effluent and so on), which we hope will motivate further technological advancements in the future.

## Methods

**Synthesis of Cu-$C_3N_4$.** Typically, 2 g of 50 wt.% cyanamide aqueous solution (Alfa-Aesar) and 0.287 g of $Cu(NO_3)_2{\cdot}3H_2O$ (Sigma-Aldrich) were added to a 10-ml glass vial. The mouth of the vial was covered by a piece of aluminum foil with four fine holes poked in it. The vial was then placed in a muffle furnace, heated to 550 °C over 40 min and maintained at this temperature for 1 h. The Cu content in Cu-$C_3N_4$ can be tailored by altering the mole ratio of Cu:C in the precursor.

**Fabrication of the Fenton filter.** A precursor solution was first prepared by dissolving 1.436 g of $Cu(NO_3)_2{\cdot}3H_2O$ (Sigma-Aldrich) into 10 g of 50 wt.% cyanamide aqueous solution (Alfa-Aesar). A piece of carbon felt (Alfa-Aesar) of cross-sectional area 1 $cm^2$ and length 5 cm was treated by $O_2$ plasma for 5 min and then dipped in the precursor solution; 4.5 g of the precursor solution was absorbed by the carbon felt and excess solution was gently squeezed out. The carbon felt was wrapped in a piece of aluminum foil without drying and then placed in a tube furnace, heated to 550 °C for 40 min under 1-atm Ar and maintained at this temperature for 1 h. The side faces of the carbon felt were then sealed by epoxy (Devcon 5 Minute Epoxy) and wrapped in a piece of duct tape (3 M).

**Synthesis of Cu-TMCPP.** Cu-TMCPP was synthesized according to a previous report[31], with minor modification: 3.0 g of Pyrrole (ACROS Organics) and 6.9 g of methyl p-formylbenzoate (ACROS Organics) were added to 100 ml of refluxed propionic acid (Fisher Chemical) and the solution was refluxed for 12 h with a stirring bar. Crystals were then collected by suction-filtration to afford purple crystals (TMCPP, 1.9 g, 21.3% yield). Next, 0.854 g of TMCPP and 2.2 g of $CuCl_2{\cdot}2H_2O$ (Sigma-Aldrich) were dissolved in 100 ml of dimethylformamide (Fisher Chemical) and the solution was refluxed for 6 h. After the mixture was cooled, 150 ml of deionized water was added. The precipitate thus obtained was filtered and repeatedly washed with deionized water and methanol. The solid was dissolved in $CHCl_3$, followed by washing three times with deionized water. The organic layer was dried over anhydrous magnesium sulfate (Sigma-Aldrich) and evaporated to afford dark red crystals (Cu-TMCPP).

**Synthesis of O-SP.** O-SP was synthesized according to our previous report[17], with minor modification: 0.2 g of Super P carbon black (Alfa-Aesar) and 200 ml of 12 M nitric acid (Sigma-Aldrich) were added to a three-necked, round-bottomed glass flask connected to a reflux condenser. The reaction flask, a magnetic stirrer and a thermometer were mounted in a preheated water bath. The temperature was maintained at 80 °C for 48 h. Next, the slurry was removed, cooled, centrifuged and washed with deionized water and ethanol several times until the pH was neutral. Finally, the sample was dried at 60 °C in a vacuum oven overnight.

**Fabrication of GDE.** High-density PE (Sigma-Aldrich) was mixed with ultra-high-molecular-weight PE (Alfa-Aesar) at a weight ratio of 4:1 in paraffin oil (light; Fisher Chemical) at a temperature of ~200 °C. The volume of paraffin oil was five times the weight of PE. The composite mixture was melt-pressed into a thin film at 80 °C. A piece of carbon paper (AvCarb MGL190) was then laminated with the film by melt-pressing again. Finally, the paraffin oil was extracted from the film using methylene chloride (Fisher Chemical).

**Fabrication of the $IrO_2$ anode.** $IrO_2$ was anodically electrodeposited on a titanium screen mesh according to a previous report[30], with minor modification. To prepare the electrodeposition solution, 0.15 g of $IrCl_4{\cdot}H_2O$ (Sigma-Aldrich) was dissolved in 100 ml of deionized water. Then, 0.5 g of oxalic acid (Sigma-Aldrich) and 1 ml of $H_2O_2$ aqueous solution (30 wt.%, Sigma-Aldrich) were added. After 10 min of stirring, the pH was slowly raised to 10.5 by stepwise addition of $K_2CO_3$ (Sigma-Aldrich). After preparation, the solution was heated to 90 °C for 15 min and subsequently cooled down to room temperature. Electrodeposition of $IrO_2$ was carried out by application of a constant current (0.16 mA $cm^{-2}$) on a titanium mesh (Fuel Cell Store) in a two-electrode cell for 15 min, with a graphite rod (Sigma-Aldrich) as the counter-electrode.

**Fabrication of the $Fe_3O_4$-carbon filter.** A precursor solution was first prepared by dissolving 4 g of $Fe(NO_3)_3{\cdot}9H_2O$ (Sigma-Aldrich) and 0.4 g of polyvinyl polypyrrolidone (Sigma-Aldrich) in 5.6 ml of deionized water. A piece of carbon felt (Alfa-Aesar) of cross-sectional area 1 $cm^2$ and length 5 cm was treated by $O_2$ plasma for 5 min and dipped in the precursor solution, then 4.5 g of the precursor solution was absorbed by the carbon felt. Excess solution was gently squeezed out. The carbon felt was dried at 60 °C in a vacuum oven overnight. After drying, the carbon felt was placed in a tube furnace and heated to 500 °C for 1 h under 1 atm Ar and maintained at this temperature for 1.5 h. The side faces of the carbon felt were then sealed by epoxy (Devcon 5 Minute Epoxy) and wrapped in a piece of duct tape (3 M).

**Electron microscopy.** The SEM images were taken using an FEI XL30 Sirion SEM with an acceleration voltage of 5 kV. The HR-TEM images and EDS mapping were taken by a FEI Titan 80–300 environmental (scanning) TEM operated at 300 keV. The HAADF-STEM images were taken on a TEAM 0.5 microscope operated at 300 kV. The samples were prepared by dropping catalyst powder dispersed in ethanol onto carbon-coated copper (or gold) TEM grids (Ted Pella) using micropipettes and were dried under ambient conditions. For imaging and EDS, copper and gold TEM grids, respectively, were used.

**Spectroscopy.** The Cu K-edge EXAFS spectra were collected at Beamline 4-3 of Stanford Synchrotron Radiation Lightsource. We ran Cu K-edge in the range 8.878–9.778 keV in fluorescence mode with a step size of 0.25 eV at the near edge. The XPS spectra were collected using a PHI VersaProbe Scanning XPS Microprobe with an Al (Kα) source. The FTIR spectra were measured using a Nicolet iS50 FT/IR spectrometer in attenuated total reflectance mode.

**Measurement of the catalytic activity of Cu-$C_3N_4$.** All experiments were conducted under conditions of darkness, to eliminate the effect of photocatalysis. In a typical vial experiment, 1 g $l^{-1}$ prepared catalyst powder was dispersed in 10 ml of 10 μM RhB aqueous solution. The pH was then adjusted to 7.0 using a 1 M aqueous solution of either NaOH or $H_2SO_4$. After establishment of adsorption/desorption equilibrium (10 min), 1 g $l^{-1}$ $H_2O_2$ was added to the pollutant suspension under stirring throughout the experiment. At time intervals, 1 ml of the suspension was collected and centrifuged at 10,000 r.p.m. for 30 s, then 400 μl of the supernatant was sampled and analysed immediately.

**Quantification of organic contaminants.** The pollutant concentration was measured by high-performance liquid chromatography (HPLC; Agilent 1260) equipped with a UV detector and a Zorbax Eclipse SB-C18 column (2.7 μm, 3.0 × 50 $mm^2$). The sample injection volume was 50 μl. The isocratic mobile phase contained 40% 5 mM $H_2SO_4$/60% methanol (v:v) at a flow rate of 0.7 ml $min^{-1}$. The detector wavelength was set at 554 nm for measurement of RhB, and at 665 nm for MB. The degradation products of RhB were analysed by LC–MS (Agilent 6460 Triple Quad LC–MS equipped with an Agilent 1260 LC front end). The sample injection volume was 50 μl. Samples were chromatographically separated using a Zorbax Eclipse SB-C18 column at a flow rate of 0.2 ml $min^{-1}$. The mobile phase contained 5 mM $H_2SO_4$ and methanol. The vol.% of methanol was decreased from 80 to 50 within 9 min. Electrospray ionization–mass spectrometry analysis was performed in positive mode. TOC was determined using a Shimadzu TOC-L analyser with high-temperature combustion. The concentration of $Cu^{2+}$ was measured using inductively coupled plasma mass spectrometry on a Thermo Scientific XSeries II.

**Electrochemical measurements.** The electrochemical experiments were conducted at 25 °C in an H-type electrochemical cell separated by a Nafion 117 membrane (Chemours). A Pt plate was used as the counter-electrode when testing the 2e-ORR electrode; a graphite rod (Sigma-Aldrich) was used as the counter-electrode when testing the OER electrode. Both the working and reference electrode were laid to one side of the H-type cell. A computer-controlled Bio-Logic VSP Potentiostat was used for all electrochemical experiments. CV and LSV tests were performed by sweeping the working electrode potential from open circuit potential at a scan rate of 10 mV $s^{-1}$. All the potentials were measured against a saturated calomel reference electrode (SCE) and converted to the reversible hydrogen electrode (RHE) reference: $E$ (versus RHE) = $E$ (versus SCE) + 0.240 V + 0.0591 V × pH. The potentials were also $iR$ corrected to compensate for ohmic electrolyte resistance using the $E - iR$ relation, where $i$ is current and $R$ is electrolyte resistance measured via high-frequency AC impedance.

**Quantification of $H_2O_2$.** The $H_2O_2$ concentration was measured by a traditional $Ce(SO_4)_2$ titration method based on the principle that a yellow solution of $Ce^{4+}$ will be reduced by $H_2O_2$ to colourless $Ce^{3+}$. $Ce(SO_4)_2$ solution (1 mM) was prepared by dissolving 33.2 mg of $Ce(SO_4)_2$ in 100 ml of 0.5 M $H_2SO_4$ solution. To obtain the calibration curve, $H_2O_2$ of known concentration was added to the $Ce(SO_4)_2$ solution and measured using an Agilent Cary 6000i UV/Vis/NIR Spectrometer at 316 nm. Based on the linear relationship between signal intensity and $Ce^{4+}$ concentration, $H_2O_2$ concentrations of the samples could be obtained.

**Teratogenicity studies in zebrafish embryos.** All animal procedures were performed according to National Institutes of Health (NIH) guidelines and were approved by the Committee on Administrative Panel on Laboratory Animal Care at Stanford University. Three fish culture media were prepared by adding the synthetic polluted water, the treated effluent or deionized water (blank control) to standard E3 medium at a volume ratio of 1:2. E3 medium contains 5 mM NaCl, 0.17 mM KCl, 0.33 mM $CaCl_2$ and 0.33 mM $MgSO_4$. Zebrafish zygotes were obtained from wild-type adults and cultured in standard E3 medium at 28 °C. Dead and unfertilized eggs were discarded at 4 h post fertilization (hpf), while fertilized embryos were transferred into three 10-cm culture dishes at about 120 embryos per dish. The medium was carefully removed from each dish and the embryos were then rinsed twice with 3 ml of medium containing either synthetic polluted water, treated effluent or deionized water. Each dish was then filled with 39 ml of the corresponding medium and the embryos were gently transferred to 96-well plates (one embryo in 300 µl of medium per well) and cultured at 28 °C. Embryo development was monitored, and representative images were acquired at 24, 48, 72, 96, 120 and 144 hpf.

## Data availability

The data that support the findings of this study are available from the corresponding author upon request.

Received: 17 July 2019; Accepted: 6 October 2020;
Published online: 09 November 2020

## References

1. Miklos, D. B. et al. Evaluation of advanced oxidation processes for water and wastewater treatment—a critical review. *Water Res.* **139**, 118–131 (2018).
2. Chuang, Y.-H., Chen, S., Chinn, C. J. & Mitch, W. A. Comparing the UV/monochloramine and UV/free chlorine advanced oxidation processes (AOPs) to the UV/hydrogen peroxide AOP under scenarios relevant to potable reuse. *Environ. Sci. Technol.* **51**, 13859–13868 (2017).
3. Hodges, B. C., Cates, E. L. & Kim, J.-H. Challenges and prospects of advanced oxidation water treatment processes using catalytic nanomaterials. *Nat. Nanotechnol.* **13**, 642–650 (2018).
4. Glaze, W. H., Kang, J.-W. & Chapin, D. H. The chemistry of water treatment processes involving ozone, hydrogen peroxide and ultraviolet radiation. *Ozone Sci. Eng.* **9**, 335–352 (1987).
5. Katsoyiannis, I. A., Canonica, S. & von Gunten, U. Efficiency and energy requirements for the transformation of organic micropollutants by ozone, $O_3/H_2O_2$ and UV/$H_2O_2$. *Water Res.* **45**, 3811–3822 (2011).
6. Neyens, E. & Baeyens, J. A review of classic Fenton's peroxidation as an advanced oxidation technique. *J. Hazard. Mater.* **98**, 33–50 (2003).
7. Nidheesh, P. V. Heterogeneous Fenton catalysts for the abatement of organic pollutants from aqueous solution: a review. *RSC Adv.* **5**, 40552–40577 (2015).
8. Pham, A. L.-T., Lee, C., Doyle, F. M. & Sedlak, D. L. A silica-supported iron oxide catalyst capable of activating hydrogen peroxide at neutral pH values. *Environ. Sci. Technol.* **43**, 8930–8935 (2009).
9. Lyu, L., Zhang, L., Wang, Q., Nie, Y. & Hu, C. Enhanced Fenton catalytic efficiency of γ-Cu–$Al_2O_3$ by σ-$Cu^{2+}$–ligand complexes from aromatic pollutant degradation. *Environ. Sci. Technol.* **49**, 8639–8647 (2015).
10. Costa, R. C. C. et al. Novel active heterogeneous Fenton system based on $Fe_{3-x}M_xO_4$ (Fe, Co, Mn, Ni): the role of $M^{2+}$ species on the reactivity towards $H_2O_2$ reactions. *J. Hazard. Mater.* **129**, 171–178 (2006).
11. Gao, L. et al. Intrinsic peroxidase-like activity of ferromagnetic nanoparticles. *Nat. Nanotechnol.* **2**, 577–583 (2007).
12. Navalon, S., Alvaro, M. & Garcia, H. Heterogeneous Fenton catalysts based on clays, silicas and zeolites. *Appl. Catal. B* **99**, 1–26 (2010).
13. Navalon, S., Dhakshinamoorthy, A., Alvaro, M. & Garcia, H. Heterogeneous fenton catalysts based on activated carbon and related materials. *ChemSusChem* **4**, 1712–1730 (2011).
14. Bataineh, H., Pestovsky, O. & Bakac, A. pH-induced mechanistic changeover from hydroxyl radicals to iron(IV) in the Fenton reaction. *Chem. Sci.* **3**, 1594–1599 (2012).
15. Lin, S.-S. & Gurol, M. D. Catalytic decomposition of hydrogen peroxide on iron oxide: kinetics, mechanism, and implications. *Environ. Sci. Technol.* **32**, 1417–1423 (1998).
16. Campos-Martin, J. M., Blanco-Brieva, G. & Fierro, J. L. G. Hydrogen peroxide synthesis: an outlook beyond the anthraquinone process. *Angew. Chem. Int. Ed. Engl.* **45**, 6962–6984 (2006).
17. Lu, Z. et al. High-efficiency oxygen reduction to hydrogen peroxide catalysed by oxidized carbon materials. *Nat. Catal.* **1**, 156–162 (2018).
18. Kim, H. W. et al. Efficient hydrogen peroxide generation using reduced graphene oxide-based oxygen reduction electrocatalysts. *Nat. Catal.* **1**, 282–290 (2018).
19. Siahrostami, S. et al. Enabling direct $H_2O_2$ production through rational electrocatalyst design. *Nat. Mater.* **12**, 1137–1143 (2013).
20. Choi, C. H. et al. Tuning selectivity of electrochemical reactions by atomically dispersed platinum catalyst. *Nat. Commun.* **7**, 10922 (2016).
21. Xia, C., Xia, Y., Zhu, P., Fan, L. & Wang, H. Direct electrosynthesis of pure aqueous $H_2O_2$ solutions up to 20% by weight using a solid electrolyte. *Science* **366**, 226–231 (2019).
22. Chen, Z. et al. Development of a reactor with carbon catalysts for modular-scale, low-cost electrochemical generation of $H_2O_2$. *React. Chem. Eng.* **2**, 239–245 (2017).
23. Murayama, T. & Yamanaka, I. Electrosynthesis of neutral $H_2O_2$ solution from $O_2$ and water at a mixed carbon cathode using an exposed solid-polymer-electrolyte electrolysis cell. *J. Phys. Chem. C.* **115**, 5792–5799 (2011).
24. Yamanaka, I. & Murayama, T. Neutral $H_2O_2$ synthesis by electrolysis of water and $O_2$. *Angew. Chem. Int. Ed. Engl.* **47**, 1900–1902 (2008).
25. Bojdys, M. J., Müller, J.-O., Antonietti, M. & Thomas, A. Ionothermal synthesis of crystalline, condensed, graphitic carbon nitride. *Chemistry* **14**, 8177–8182 (2008).
26. Liu, J., Zhang, T., Wang, Z., Dawson, G. & Chen, W. Simple pyrolysis of urea into graphitic carbon nitride with recyclable adsorption and photocatalytic activity. *J. Mater. Chem.* **21**, 14398–14401 (2011).
27. Natarajan, T. S., Thomas, M., Natarajan, K., Bajaj, H. C. & Tayade, R. J. Study on UV-LED/$TiO_2$ process for degradation of rhodamine B dye. *Chem. Eng. J.* **169**, 126–134 (2011).
28. He, Z. et al. Photocatalytic degradation of rhodamine B by $Bi_2WO_6$ with electron accepting agent under microwave irradiation: mechanism and pathway. *J. Hazard. Mater.* **162**, 1477–1486 (2009).
29. Fu, H., Pan, C., Yao, W. & Zhu, Y. Visible-light-induced degradation of rhodamine B by nanosized $Bi_2WO_6$. *J. Phys. Chem. B* **109**, 22432–22439 (2005).
30. Yamanaka, K. Anodically electrodeposited iridium oxide films (AEIROF) from alkaline solutions for electrochromic display devices. *Jpn. J. Appl. Phys.* **28**, 632 (1989).
31. Feng, D. et al. Zirconium-metalloporphyrin PCN-222: mesoporous metal–organic frameworks with ultrahigh stability as biomimetic catalysts. *Angew. Chem. Int. Ed. Engl.* **51**, 10307–10310 (2012).

## Acknowledgements

Part of this work was performed at the Stanford Nano Shared Facilities, supported by the National Science Foundation under award no. ECCS-1542152. Use of the Stanford Synchrotron Radiation Lightsource, SLAC National Accelerator Laboratory, was supported by the US Department of Energy, Office of Science, Office of Basic Energy Sciences under contract no. DE-AC02-76SF00515. Work at the Molecular Foundry was supported by the Office of Science, Office of Basic Energy Sciences, of the US Department of Energy under contract no. DE-AC02-05CH11231. The teratogenicity experiment was supported by NIH grant no. R35 GM127030.

## Author contributions

J.X. and Y.C. conceived the idea. J.X. performed the experiments. X.Z. performed the EXAFS and STEM characterizations. Z.F. performed the teratogenicity studies. Z.L. synthesized the O-SP. W.H., Y.L. and Z.Z. performed the HR-TEM and EDS characterizations. D.V. and Y.L. helped with the HPLC and LC–MS measurements. S.D. helped with the STEM characterizations. K.W. synthesized Cu-TMCPP. Z.L. and G.C. helped with quantification of $H_2O_2$. H.W. and Z.Z. helped with electrochemistry experiments. J.X. and Y.C. wrote the manuscript with input from all co-authors.

## Competing interests
The authors declare no competing interests.

## Additional information
**Supplementary information** is available for this paper at https://doi.org/10.1038/s41893-020-00635-w.

**Correspondence and requests for materials** should be addressed to Y.C.

**Reprints and permissions information** is available at www.nature.com/reprints.

**Publisher's note** Springer Nature remains neutral with regard to jurisdictional claims in published maps and institutional affiliations.

© The Author(s), under exclusive licence to Springer Nature Limited 2020